Detailed Spatial Slip Distribution for Short-term Slow Slip Events along the Nankai Subduction Zone, Southwest Japan

Masayuki Kano[1] (ORCID: 0000-0002-7288-4760) **and Aitaro Kato**[2] (ORCID: 0000-0002-2645-3441)

[1]Graduate School of Science, Tohoku University, Sendai, Japan.

[2]Earthquake Research Institute, the University of Tokyo, Tokyo, Japan.

Corresponding author: M. Kano (email: masayuki.kano.a3@tohoku.ac.jp)

Key Points: (140 char.)

- Detailed cumulative slip distribution for short-term slow slip events (S-SSEs) is estimated in the Nankai subduction zone, southwest Japan (140)
- S-SSEs are inferred not only deep transition zones but shallow areas along the plate interface in eastern Shikoku and Tokai (124)
- Large slip areas of S-SSEs are possibly separated in space from the active areas of low-frequency earthquakes (111)

Abstract

Short-term slow slip events (S-SSEs) intensively occur at the transition zone along the Nankai subduction zone, southwest Japan. Because crustal deformation due to a single S-SSE is small, the source fault is often represented using a planar uniform single-fault slip model, resulting to little constraint on the spatial heterogeneity in amounts of fault slip. To comprehensively investigate the detailed cumulative spatial distribution of S-SSEs in the entire Nankai subduction zone, we adopted a stacking approach of Global Navigation Satellite System (GNSS) data using low-frequency earthquakes as reference. We extracted cumulative displacements due to a series of S-SSEs from 2004 to 2009; coherent signals in almost opposite direction of plate subduction were obtained. The inverted slip indicated significant slip patches laterally elongated along the transition zone at ~30–35 km depth, and small patches in the shallow portions at ~15–20 km and ~10–15 km depth in eastern Shikoku and in Tokai as well as western Shikoku, respectively. The shallow patches in Shikoku were located on the downdip edge of the coseismic slip area of the 1946 Nankai earthquake, while the Tokai small slip was located on the shallower side of the anticipated source area of a large earthquake. Large slip patches of S-SSEs were complementary to the spatially dense low-frequency earthquake areas; in major S-SSE areas, the number of low-frequency earthquakes is small. This spatial dependence of fault slip style even within the transition zone provides new insights regarding the generation mechanism of slow earthquakes.

1. Introduction

In these decades, slow earthquakes characterized by longer duration compared to ordinary earthquakes (Ide et al., 2007) have been discovered one after another in tectonic zones worldwide (e.g., Schwartz & Rokosky, 2007; Obara & Kato, 2016). Although slow earthquakes alone do not result in significant seismic damage because of their slow fault rupture, their source locations have been often identified near seismogenic zones where huge earthquakes previously occurred or are expected to occur. Thus, slow earthquakes can perturb seismiogenic zones by loading tectonic stress. In fact, prior to large earthquakes, slow earthquake have been often observed adjacent to their source areas (Graham et al., 2014; Ito et al., 2013; Kato et al., 2012; Ozawa et al., 2012; Radiguet et al., 2016; Ruiz et al., 2014; Socquet et al., 2017; Voss et al., 2018; Yokota & Koketsu, 2015). Therefore, investigating activities of slow earthquakes provides important information regarding tectonic processes during earthquake cycles.

Among the various types of slow earthquakes, slow slip events (SSEs) are geodetic signatures of slow fault rupture that are fundamentally recognized by observing slow crustal deformation using geodetic instruments such as Global Navigation Satellite System (GNSS) (Hirose et al., 1999), tiltmeters (Sekine et al., 2010), strainmeters (Itaba et al., 2010), ocean bottom pressure gauges (Ito et al., 2013; Wallace et al., 2016), and Synthetic Aperture Radar (Hooper et al., 2012; Bekaert et al., 2015). SSEs are often classified into two types depending on their durations: long-term SSEs (L-SSEs) last for months to years (Hirose et al., 1999), whereas short SSEs (S-SSEs) last for days to weeks (Obara et al., 2004). The amplitudes of crustal deformations associated with L-SSEs are sufficiently large, and can be used in investigating their source processes (Ozawa et al., 2001). On the other hand, those of S-SSEs are often too small, and can be hidden in the background observational noise. The extraction of such small signals is an important issue for capturing the features of S-SSE activities.

Several studies have developed the methodology to extract small crustal deformation due to S-SSEs (Bartlow, 2020; Frank, 2016; Frank et al., 2015; Haines et al., 2019; Nishimura et al., 2013; Rousset et al., 2017). One approach is fitting a specific function to the GNSS data. Nishimura et al. (2013) assumed a linear function with and without a step due to an S-SSE and comprehensively detected S-SSEs in the Nankai subduction zone, southwest Japan, when linear functions with a step better explained the observation data in terms of Akaike's information criteria. Another approach is stacking GNSS data to increase the signal-to-noise ratio by compromising on temporal resolution. Frank et al. (2015) utilized low-frequency earthquakes (LFEs) as an in situ monitoring tool of SSEs, assuming that the quantity of LFEs reflects a background slow fault slip, to extract signals from a series of S-SSEs in the Guerrero subduction, Mexico. When LFE bursts occurred, detrended GNSS displacements were stacked, following which cumulative surface displacement for seven episodes were obtained. They clarified that the locations of S-SSEs are deeper than L-SSEs. This stacking approach is useful in capturing the overall spatial characteristics of S-SSEs.

In the Nankai subduction zone (Fig. 1), the Philippine Sea plate subducts beneath the Amurian plate at a rate of ~67 mm yr^{-1} (Miyazaki & Heki, 2001). Large megathrust earthquakes with moment magnitudes (M_w) of ~8 rupture the plate interface at a depth of < ~20 km with a recurrence interval of 90–200 years (Ando, 1975). L-SSEs with M_w of ~7 repeatedly inferred below the seismogenic zone at the Bungo Channel (Hirose et al., 1999; Ozawa et al., 2013), Kii Channel (Kobayashi, 2014), and Tokai area (Miyazaki et al., 2006; Ochi & Kato, 2013; Ozawa et al., 2016). In addition, relatively smaller (M_w of ~6.0–6.6) L-SSEs are identified just below the seismogenic zone in western Shikoku (Takagi et al., 2019). These L-SSEs lasted for a duration of months and are usually detectable by GNSS observation. On the deeper side of these L-SSEs, S-SSEs with M_w of 5.4–6.2 frequently occur at ~35 km depth at intervals of several months (Hirose & Obara, 2010), concordant with the

tectonic tremors referred to as episodic tremor and slip (ETS) (Obara et al., 2004). Since the magnitude of crustal deformation due to S-SSEs was small, tiltmeters were usually utilized to identify S-SSEs and to elucidate a spatio-temporal evolution of the slip during a few major S-SSEs (Hirose & Obara, 2010; Obara et al., 2004; Sekine et al., 2010). With the advancements in detection methods (Nishimura et al., 2013), GNSS data became recently available to identify small signals of S-SSEs and source locations of more than 100 S-SSEs have been estimated over 15 years. However, the source locations were determined as a single planar rectangular fault model assuming a spatially uniform slip. Therefore, the detailed spatial distributions of the slip from S-SSEs were not clarified. In addition, it is difficult to estimate multiple source locations in principle.

To comprehensively investigate the spatial distribution of S-SSEs, Kano et al. (2019) applied the stacking method (Frank et al., 2015) to the GNSS data in western Shikoku, and succeeded to extract the cumulative displacements due to 12 S-SSEs previously detected by GNSS (Nishimura et al., 2013) and/or tiltmeters (Sekine et al., 2010). The inverted slip indicated two slip patches: a large patch at ~35 km depth and a small patch at ~20 km depth. The deep large patch was located at a well-documented ETS source area in previous studies (Hirose et al., 2010; Nishimura et al., 2013; Sekine et al., 2010). The estimated seismic moment was comparable to that expected from these studies, showing the applicability of the stacking method of Frank et al. (2015). Additionally, a small but significant slip was simultaneously inferred at the bottom of the strongly coupled region where little interseismic slip was previously considered to occur. This shallow slow slip transient was possibly excited by the ETS episodes and may reflect the unlocking process of the seismogenic zone. This finding was attributed to the detailed estimation of the slip of a series of S-SSEs. Following the case study in western Shikoku (Kano et al., 2019), this study aims to image the detailed

cumulative spatial distribution of S-SSEs in the entire Nankai subduction zone, i.e., eastern Shikoku, Kii, and Tokai regions (Fig. 1), and discuss the overall features of S-SSEs.

2. Extraction of GNSS signals due to S-SSEs

This study attempts to extract cumulative GNSS displacements due to 12, 11, and 14 S-SSEs with LFE bursts in eastern Shikoku, Kii, and Tokai region from April 2004 to March 2009 (Table 1), respectively, which have been already identified through the analysis of tiltmeters (Sekine et al., 2010) and/or GNSS (Nishimura et al., 2013). The signal extraction is conducted by referencing the numbers of LFEs using the stacking method originally proposed by Frank et al. (2015), and the detailed procedures of the method is the same as Kano et al. (2019) that adopted Frank et al. (2015)'s method to the S-SSEs in western Shikoku.

Firstly, we defined the reference date for each S-SSE when maximum number of LFEs occurred during the period of 5 days before and 15 days after the onset of each S-SSE determined by Sekine et al. (2010) and/or Nishimura et al. (2013) (Table 1). The LFE catalog was systematically obtained by the matched-filter technique (Shelly et al., 2007; Kato et al., 2013) utilizing waveforms of template events detected by the Japan Meteorological Agency (the details of estimation are summarized in Kano et al., 2019). We used continuous three-component velocity seismograms retrieved by a nationwide high-sensitivity seismograph network (Hi-net) from April 2004 to March 2009. As template events, we selected 4,219 LFEs in southwest Japan (from western Shikoku to Tokai regions) with relatively high signal-to-noise ratios as identified by the Japan Meteorological Agency (JMA). The continuous and template waveforms were preprocessed by using bandpass filtering between 2 and 6 Hz and decimating the sampling from 100 to 20 Hz. We then extracted a 6.0 s data window, starting 3.0 s prior to the arrival of synthetic S-wave. The synthetic arrivals were

calculated using the one-dimensional velocity structure of the JMA. The event detection threshold was set at 9 times the median absolute deviation of the average correlation coefficient calculated over the day of interest. We assigned the location of the detected event to that of a template event. For multiple detections in each ±6.0 s window, we used the template event location with the highest mean correlation coefficient. After removing multiple detections, we detected ~220,000 LFEs located at 30–35 km depths with some clusters during our analysis, (Fig. 2). The obtained LFE catalog was referred to determine the reference dates as the center of the period for stacking the GNSS time series.

The daily crustal movements on the Earth's surface have been monitored by the GNSS Earth Observation Network System (GEONET) in Japan, which has been operated by the Geospatial Information Authority of Japan (GSI) since 1997. We analyzed the GEONET F3 solution (Nakagawa et al., 2009) to obtain the daily coordinates in two horizontal components at 49, 54, and 76 stations in eastern Shikoku, Kii, and Tokai regions, respectively, for the following analysis (Fig. 2). After correcting the offsets due to antenna displacements and large earthquakes, the daily coordinates averaged over the three stations (0462, 0691, and 0692 in Fig. 1) in the islands of west-off Kyushu, were subtracted from time series in each station. This indicates the removal of common mode errors from the original time series and the resulting daily displacements are the movement relative to the Amurian plate. Then, we calculated the 20-day moving averages for each time series. After preprocessing, we focused on the 300-day period based on the reference date for each S-SSE and subtracted the linear trend in each GNSS time series. Finally, the detrended time series were respectively stacked over the multiple SSEs in each region. Figure 2 summarizes examples of stacked GNSS time series, showing a transient movement around day 150. The time series for the other stations can be seen in Figs. S1–S3. This stacking approach by increasing the signal-to-noise ratio

158 enables the extraction of the cumulative displacements due to S-SSEs as already verified in
159 Guerrero (Frank et al., 2015) and western Shikoku (Kano et al., 2019).

160 Displacements due to a series of S-SSEs defined as the differences of the stacked time
161 series between days 140 and 160 are shown in Fig. 2. The ellipsoids in each vector indicate a
162 standard deviation of the residuals calculated by respectively fitting the linear trend to the
163 stacked time series from days 50 to 100 and days 200 to 250. In eastern Shikoku, most of the
164 stations exhibit coherent south to southeast signals. The amplitude of displacement vectors
165 are large in southeastern part of the region with a maximum amplitude of ~0.94 cm at station
166 0423 (Fig. 2a). The displacement vectors in Kii are oriented from southwest to southeast and
167 are more scattered compared to those in eastern Shikoku (Fig. 2b). Large signals of ~0.6–0.8
168 cm can be identified at stations above the isodepth contour of ~30 km. GNSS stations located
169 in the western part of Tokai moves southeast, while those in the eastern part moves eastward
170 (Fig. 2c). The magnitudes of displacements are relatively large (~0.6 cm) around stations
171 0303 and 3097. The extracted displacement vectors lie in a direction nearly opposite to that of
172 the subduction of the Philippine Sea plate relative to the Amurian plate. Therefore, we
173 considered these signals as originating from tectonic processes.

174

175 **3. Estimation of cumulative spatial distribution of S-SSEs**

176 **3.1. Inversion analysis**

177 The surface displacements extracted in the previous section are projected onto a
178 cumulative fault slip on the plate interface following the inversion scheme of Nishimura
179 (2009). Firstly, we generated a model of the geometry of the upper surface of the subducting
180 Philippine Sea plate using the depth contours of the plate interface estimated by Baba et al.

(2002), Hirose et al. (2008), and Nakajima & Hasegawa (2007). Then, the plate interface was divided into planar subfaults in both strike and dip directions so that each modeled region respectively covers the whole eastern Shikoku, Kii, and Tokai regions. Each subfault was determined to be 7.5 × 7.5 km when projected on the ground surface. The numbers of subfaults were 24 × 21 in eastern Shikoku, 26 × 17 in Kii, and 25 × 21 in Tokai. Additional subfaults with zero slip were assigned surrounding the model fault region that are not represented in each figure. As a prior constraint, spatial smoothing of slip in adjacent faults for both strike and dip directions was adopted. With spatial smoothing and additional zero slip subfaults, the estimated slip varied smoothly and the slip at the edge of the model region became smaller. The slip direction of each subfault was fixed at N125E, which is in an approximately an opposite direction of the subduction of the Philippine sea plate relative to the Amurian plate (Miyazaki & Heki, 2001); thus, the rake angles in each subfault were adjusted to match the slip direction. The displacement response on the Earth's surface at the GNSS stations due to a unit fault slip on each subfault was calculated by assuming an elastic homogenous half-space (Okada, 1992). With this setting, the amounts of slip and their corresponding errors were estimated via the following equations:

$$s(\mathbf{a}) = (\mathbf{d} - \mathbf{H}\mathbf{a})^{\mathrm{T}}\mathbf{E}^{-1}(\mathbf{d} - \mathbf{H}\mathbf{a}) + \alpha^2\mathbf{a}^{\mathrm{T}}\mathbf{G}\mathbf{a}, \tag{1}$$

$$\mathbf{C} = \frac{s(\hat{\mathbf{a}})}{(N + P - M)}(\mathbf{H}^{\mathrm{T}}\mathbf{E}^{-1}\mathbf{H} + \alpha^2\mathbf{G})^{-1}, \tag{2}$$

where **d** is the observed displacement vector, **H** is the matrix consisting of an elastic response, **a** is the model parameter (the amounts of slips), **E** is the covariance matrix for the observed errors, and **G** is the smoothing operator. The slip distributions were optimized by minimizing equation (1) consisting of a data misfit and smoothness constraint terms. The hyperparameter α^2 that controls the balance of the data misfit and spatial smoothing terms is determined by minimizing Akaike's Bayesian information criterion (Akaike, 1980). The estimation errors

for the obtained slip are the diagonal elements of the error covariance matrix **C**, which are calculated using the optimum model parameter $\hat{\mathbf{a}}$ by equation (2), where N is the number of GNSS data, P is the rank of the smoothing operator **G**, and M is the number of model parameters to be determined. This inversion scheme was adopted individually for the observed vectors in eastern Shikoku, Kii, and Tokai regions (Fig. 2) to estimate the cumulative spatial distributions of S-SSEs.

3.2. Eastern Shikoku

The spatial distribution of cumulative fault slip due to 12 S-SSEs in eastern Shikoku (Fig. 3a) showed several slip patches. Focusing on the slips that exceeded their estimation errors (Fig. 3b), we identified one large slip patch (E1) and five relatively smaller patches (E2–E6). For all subfaults exceeding the errors, a cumulative seismic moment of 100.4×10^{17} Nm corresponding to M_w 6.60 was calculated by assuming a rigidity of 40 GPa. The displacement vectors calculated from the estimated slip on all subfaults showed good agreement with the observed data (Fig. 3c).

E1 patch is elongated at a depth of ~30 km in the strike direction with the maximum slip of ~5.5 cm located on its eastern side. E2 patch is located on the western side of E1 patch at a similar depth. The source areas of these patches are identified within the ETS zone and are roughly consistent with the rectangular fault models inferred by Sekine et al. (2010) and Nishimura et al. (2013). A total seismic moment of 64.1×10^{17} Nm (M_w 6.47) is obtained summing up the subfaults exceeding 1-σ estimation errors (hereafter, the seismic moment values or M_w indicate only the contributions of the subfaults where their slips exceeded the 1-σ estimation errors in the regions of interest). This value is approximately half of that estimated by summing up the previously estimated values of 118.1×10^{17} Nm (M_w 6.65) in

Sekine et al. (2010) and Nishimura et al. (2013). This difference may be attributed to the estimation discrepancy of the fault model since we assumed a detailed spatial distribution of the slip, while previous studies assumed a uniform slip model with a single fault.

The other four small patches (E3–E6) are identified outside the ETS zone. To confirm the validity of their estimated slips, we conducted additional jackknife test with random resampling technique. We performed inversion analysis for 100 cases using the displacements at randomly selected 39 stations, i.e., 80 % of the total stations and estimated the average slip distributions and their standard deviations for 100 cases (Figs. 3d & 3e). The slip areas indicated by the average slip distribution were almost similar to those obtained by all 49 stations (Fig. 3a). However, there are less peak slips in small patches (E2–E6), especially in E6 patch where the peak slip decreased to ~37 % of the initial amount. If a slip in a patch is sensitive only to a few stations and its observed vectors there are not used for inversion in the jackknife test, the estimated slip in the patch becomes smaller, resulting in a smaller average slip than that when all stations are used. Therefore, we considered that the fault slip in E6 patch largely relied on a small number of stations.

To investigate the detectability of the small slip patches E3–E6, we calculated the surface displacement due only to the slip within each individual patch (Fig. 4). For E3 patch (Fig. 4a), the fault slip is hardly detectable even in the stations near the patch which moves < 1.0 mm because the slipping area is deep (> 40 km). On the other hand, E4–E6 patches are located at the shallower depth of ~15–20 km. The transient slip in E4 patch ranged ~1.8–2.7 cm with a moment magnitude of 8.5×10^{17} Nm (M_w 5.89). Although the amount of slip is small, the shallow fault depth resulted in surface displacements of > 2 mm at four GNSS stations, comparable to 2-σ observation errors (Fig. 4b). At these stations near the eastern coast line, the slips in E4 patch explained one-fourth to one-third of the total calculated displacements in their amplitudes (Fig. 3c). In addition, the standard deviations of the fault

slip in E4 patch is relatively smaller within the entire fault (Fig. 3e) with more significant estimated slips of ~1.8–2.7 cm compared to their standard deviations. Therefore, despite its weak detection, a small amount of transient slip likely occurred in this shallow small E4 patch, which can explain the observed vectors in the southeastern part of the Shikoku region. E5 patch is located on the western side of E4 patch. However, even though the slip patch exists at a shallow depth, its slip is too small (~2 cm) to be detected as a signal at stations close to the patch (Fig. 4c). There are relatively larger fault slips (2.1–4.6 cm) in E6 patch located offshore the southwestern edge of the fault region. The surface displacements of ~2–4 mm due to this patch (Fig. 4d) are comparable to the 2-σ observation errors at the three southern stations. In two of these stations, quite a large fraction (87–99 %) of the amplitudes of the calculated vectors due to all subfaults (Fig. 3b) can be explained by the slip in E6 patch. This means, as mentioned in the last paragraph, the amount of fault slip in E6 patch largely depends on whether the observed vectors at these two stations are utilized in the inversion. Additional analyses using more S-SSEs during a longer period and more stations in the western part will improve the signal-to-noise ratio to support any shallow slip in E6 patch if it exists. However, this is beyond the scope of the present study.

3.3 Kii

In the Kii region, spatial distribution accumulated for 14 S-SSEs consists of an eastern large patch (K1) and a western small patch (K2) (Figs. 5a and 5b), with a cumulative seismic moment of 82.6×10^{17} Nm corresponding to M_w 6.54. The estimated slip distribution quantitatively reproduced the displacement vector that matched the observed vectors (Fig. 5c).

The large patch K1 is located at depths of ~35 km elongating to ~110 km in the strike direction. In K1 patch, two peak slips are estimated – a peak slip of ~6.9 cm at its center and ~5.8 cm at its northeastern edge of below the Ise Bay. The source region of K1 patch

corresponded to the ETS zone where the source models were inferred by Sekine et al. (2010) and Nishimura et al. (2013). A total seismic moment of 116.6 × 10^{17} Nm (M_w 6.64) is obtained, roughly comparable to that of our inversion result of 77.2 × 10^{17} Nm (M_w 6.53). In addition, the slip zone extended to deeper faults (> 40 km depth) at the southwestern edge of K1 patch. The slips of 2.0–3.9 cm are relatively smaller than those in the shallower slip region.

At a location southwest of K1 patch, a small slip patch (K2) at ~40 km depth is observed. K2 patch is slightly deeper than the previously inferred source area in western Kii. However, it rarely contributed to the calculated displacements (< 0.6 mm) that are smaller than the 2-σ observation errors (Fig. 5d); thus, it is not further discussed in the present study.

3.4. Tokai

We derived a cumulative slip distribution for 11 S-SSEs in the Tokai region (Figs. 6a & 6b), where two major slip patches were imaged (T1 & T2). The displacement vectors calculated from all subfaults showed a good agreement with those from observations (Fig. 6c).

The large slip in T1 patch locating eastern side of the Ise Bay occurred at a depth of ~ 30 km with amplitudes of ~ 5.0 cm. The slip zone extended to ~ 80 km in the strike direction within the ETS zone and ~ 80 km in the dip direction up to a depth ~ 40 km. A seismic moment of 67.7 × 10^{17} Nm (M_w 6.49) was obtained in T1 patch. The source region and seismic moment are consistent with those detected by Sekine et al. (2010) and Nishimura et al. (2013) shown by blue rectangles in Fig. 6a with a seismic moment of 68.3 × 10^{17} Nm (M_w 6.49). In addition, the ETS zone is complementary distributed on the deeper side of L-SSE, which mainly slips below the western side of Lake Hamana (Fig. 5b) (Miyazaki et al., 2006; Ozawa et al., 2016), indicating a depth dependence of the slip style.

303 Notably, a small fault slip is inferred in a wide area off Cape Omaezaki at shallow
304 depths of 10–15 km (T2 patch). This slip patch caused significant crustal movement of > 2
305 cm at 11 stations exceeding the 2-σ observation errors (Fig. 6d). To further confirm this slip
306 in T2 patch, additional slip inversion is performed for 100 cases, randomly selecting 80 % of
307 the total stations (61 stations) (jackknife test). The slip distribution averaged for 100 cases
308 (Fig. 6e) is quite similar to that using all observed displacements (Fig. 6a) in terms of the
309 overall characteristics and quantity of slips even in T2 patch. However, the standard
310 deviations of the slip at the northern part of T2 patch is slightly larger (~ 0.6 mm). The above
311 validation suggests that the GNSS stations densely distributed around Cape Omaezaki
312 contributed in illuminating the small but significant slip in T2 patch on the shallow depth of
313 the plate interface.
314

315 **4 Discussion**

316 **4.1 Shallow slip patches**

317 Figure 7 summarizes the cumulative slip distributions for S-SSEs detected from 2004
318 to 2009 in southwest Japan revealed by Kano et al. (2019) (western Shikoku) and in this
319 study (eastern Shikoku, Kii, and Tokai). The main slip areas are laterally elongated in the
320 ETS zone, while shallow minor patches are inferred in western and eastern Shikoku and
321 Tokai areas.

322 In eastern Shikoku, the small slip patch (E4 patch) is estimated to be present just
323 updip side of the L-SSE source area in the Kii Channel (Fig. 3b), where M_w 6.6–6.7 class L-
324 SSEs occurred repeatedly in 1996–1997 (Kobayashi, 2014), 2000–2003 and 2014–2017
325 (Kobayashi, 2017). During our analysis period, there have been no reports of L-SSEs; hence,
326 we cannot discuss any temporal correlation between L-SSE region and E4 patch. However,

both source regions do not seem to overlap at the plate interface. The slow slip transient in the E4 patch occurs within the moderately coupled region with a slip deficit rate of ~ 2–3 cm yr^{-1} (Yokota et al., 2016; Nishimura et al., 2018) and the area which experienced a relatively smaller coseismic slip in 1946 Nankai earthquake (Figs. 1 & 3b) (Sagiya & Thatcher, 1999). This suggests that small slow slip transient sometimes causes gradual unlocking at the bottom of the strongly coupled zone. Similar transient slow slip has been also inferred in western Shikoku region (W1 patch in Fig. 7) (Kano et al., 2019).

The shallow slip transients occur without LFEs in eastern and western Shikoku (Fig. 7). The small S-SSEs that were not associated with LFEs below the locked megathrust were also identified in northern Cascadia (Hall et al., 2018). The slow slip extends ~ 15 km to the updip side of the ETS zone. Hall et al. (2018) proposed that the lack of LFEs on the updip S-SSEs can be explained by an along-dip variation of rheological properties and/or fault strength. These two mechanisms expect along-dip changes of frictional properties or effective normal stress and thus, such mechanisms would explain the preference for slow slip instead of LFEs on the shallow slip patches in eastern and western Shikoku.

In addition, because our method extracts GNSS signals generated due to known ETS episodes at a depth of ~ 30 km, the subfaults in the shallower E4 patch simultaneously move with those in the deep E1 patch. Considering that the observed vectors are obtained from the difference of displacements during 20 days and that the stacked GNSS data is smoothed using 20-days moving averages, a time lag of slow slip occurrence between E1 and E4 patches is at most a few tens of days. Although we cannot conclusively ascertain the mechanisms functioning here, direct stress transfer from E1 patch to E4 patch or an updip fluid migration along the plate interface as proposed in the case of western Shikoku (Kano et al., 2019) may explain this almost simultaneous occurrence of transient slip.

While the small slip patches are estimated on the downdip portion of the locked megathrust region in eastern and western Shikoku, the small slip patch (T2 patch) is estimated within the shallower portion of the anticipated source area of Tokai earthquake (Figs. 1 & 6b) that is proposed by the Central Disaster Management Council (2001) where no large M~8 class earthquakes have occurred for more than 150 yrs (Ando, 1975). This small slip transient may represent a cumulative slip of shallow S-SSEs that are first revealed in Tokai region. In the off-Kii region, several shallow S-SSEs with slips of 1–4 cm were recurrently detected at depths of 4–10 km on the offshore side of the rupture area of the M_w 8.1 Tonankai earthquake, which occurred in 1944 (Fig. 1), as pore pressure changes at the seafloor borehole stations (Araki et al., 2017). These shallow S-SSEs contribute to releasing 30–55 % of stress accumulation due to the plate subduction near the trench. On the other hand, the fault slips in T2 patch ranging from 0.7 to 1.5 cm for 5 yrs accommodate 5–15 % of relative plate motion of 2–3 cm/yr in Tokai (Miyazaki & Heki, 2001), which is smaller than the off-Kii region. However, because the estimated slip is accumulated only for the period of S-SSEs occurrence in the deeper portion within the ETS zone, we may underestimate the slip amount of the shallow S-SSEs. Recent onshore and offshore geodetic studies indicated a smaller slip deficit rate compared to the adjacent seismogenic zone (Fig. 6b) (Yokota et al., 2016; Nishimura et al., 2018) and thus, this weaker coupling could be partly explained by the S-SSEs detected by the present study. An additional time-series analysis over a longer time period will provide further clarification regarding detailed features of the shallow S-SSE in T2 patch.

The mechanism for the simultaneous occurrence of both deep and shallow S-SSEs with a gap of anticipated seismogenic area is enigmatic. If an upward migration of over-pressurized fluid is a dominant mechanism that could trigger shallow S-SSEs during the deep S-SSEs as in the case of western Shikoku, temporal changes in pore pressure may promote

shallow minor slow slips. In western Shikoku, the spatial gap corresponds to the L-SSE source region (Takagi et al., 2019). Considering that L-SSE regions exhibit mixed fault behavior of friction and viscous deformation (Gao & Wang, 2017) and are less sensitive to the migrated fluid, Kano et al. (2019) proposed a fluid migration model as a possible mechanism. However, because unlike the case of western Shikoku, the spatial gap in Tokai corresponds to the anticipated seismogenic area, namely brittle frictional regime, and can be sensitive to fluid migration, fluid migration model is not applicable in Tokai. It may be possible that both shallow and deep S-SSEs occur independently, and the shallow S-SSEs revealed in the present study are just a fraction of the entire activity that occurred in the timing of deep S-SSEs. A time-dependent inversion analysis using a time series of a dense GNSS network consisting of GEONET and additional stations deployed around Cape Omaezaki and Lake Hamana (Sakaue et al., 2019) will reveal the detailed temporal changes in shallow S-SSEs.

4.2 Complementary distribution between large S-SSE patches and LFEs within the ETS zone

Focusing on the ETS zone at depths of ~30–35 km, the maximum slip of S-SSEs in each region is estimated to occur in locations where LFE densities calculated from the JMA catalog are low (Fig. 7). This characteristic is clear in eastern Shikoku and Tokai. The maximum slip in E1 patch occurs on the eastern side of the LFE clusters in eastern Shikoku (Fig. 3b), and the large slip is located on the western side of the LFE clusters in T1 patch in Tokai (Fig. 6b). The depths of these maximum slips are similar to those of the LFEs. In Kii, the peak slip is located between the two LFE clusters in K1 patch (Fig. 5b), and the second peak slip is located at the northeastern edge of K1 patch below the Ise Bay, where few LFEs occur. In the case of western Shikoku, the maximum slip is inferred slightly deeper side of

401 the LFE clusters. This feature means that, even at a similar depth, fault slips on the plate
402 interface in some regions are detected as geodetic signals, i.e., SSEs, while those in other
403 regions are seismically identified as LFEs.

404 From a geological standpoint, the deformation of subduction mélange shear zones is
405 related to the occurrence of SSEs and LFEs. A subduction mélange typically consists of
406 strong brittle clasts that potentially result in LFEs embedded in a weak ductile matrix
407 (Fagereng et al., 2014; Behr et al., 2018). Geological surveys have indicated that the slip
408 behavior along the plate interface in shear zones is fundamentally controlled by the ratio of
409 strong brittle clast to weak ductile matrix (Fagereng & Sibson, 2010). Beall et al. (2019)
410 demonstrated through numerical simulations that SSEs occur when the proportion of the
411 ductile matrix to the total media is high, or when force concentration of clasts is temporarily
412 inactive after clast failure even when this proportion is low. Therefore, one possible
413 explanation for complementary distribution of areas with large slips and high LFE densities
414 in the Nankai subduction zone is the spatial heterogeneity of the ratio of strong brittle clasts
415 and weak ductile matrix within the shear zones.

416 Another possibility is a spatial variation of fault instability in the framework of a rate
417 and state friction. In this framework, SSEs occur when the elastic stiffness of the surrounding
418 material is close to the critical stiffness of the fault, while the fault yields to undergo dynamic
419 brittle failure when the elastic stiffness is smaller than the critical stiffness (Ruina, 1983;
420 Yoshida & Kato, 2003). Since the critical stiffness is determined by frictional parameters and
421 effective normal stress, the spatial heterogeneity of frictional parameters or pore pressure or
422 both would be a possible mechanism for the complementary distribution of S-SSEs and LFEs.
423 Both possibilities might be feasible, and in each case, spatial heterogeneities in fault strength
424 are expected so that the spatial distribution of the preference of fault slip style might be
425 determined by the heterogeneity in fault strength.

5. Conclusions

We have herein estimated the detailed spatial slip distribution for S-SSEs in southwest Japan from 2004 to 2009. The significant SSEs are inferred along the well-known ETS zone at depths of ~30–35 km. In addition, small slow slips are estimated in offshore shallower portions such as in eastern Shikoku and Tokai. The slip deficit rates in these areas are relatively smaller than those of the adjacent strongly coupled seismogenic zone, and therefore slow slip partially releases the slip deficit accumulated along the plate interface. Especially, the shallow slip area in Tokai is located on the shallower side of the anticipated seismogenic zone, which is similar to the case of the shallow SSEs detected on the offshore side of the 1946 Tonankai earthquake revealed by Araki et al. (2017). Further analysis using GNSS time series with time-dependent geodetic inversion will more clearly reveal the detailed spatio-temporal evolutions of such small slip events. In addition, the number of LFEs is low in major slow slip areas. This represents the preference of fault slip style, i.e., whether ductile or brittle behavior is dominant depends on regions, within the transition zone where slow earthquakes occur intensively. The present results will contribute to improve the understanding of generation mechanisms of slow earthquakes.

Acknowledgments and Data

This study was supported by the JSPS KAKENHI Grant Number JP18K03796 in Grant-in-Aid for Scientific Research (C), JP16H06473, JP16H06474, JP19H04620 in Scientific Research on Innovative Areas “Science of Slow Earthquakes”, JST CREST Grant Number JPMJCR1763 and the Ministry of Education, Culture, Sports, Science and Technology (MEXT) of Japan, under its Earthquake and Volcano Hazards Observation and

Research Program. The inversion code used throughout this study was provided by T. Nishimura. We used the EIC computer system of the Earthquake Research Institute, the University of Tokyo. Generic Mapping Tools by Wessel & Smith (1998) is used to generate figures. The GEONET F3 solutions are provided by the GSI and available at http://datahouse1.gsi.go.jp/terras/terras_english.html. We use seismic data in the Hi-net (NIED, 2019) for estimating LFE locations. The JMA catalog of LFEs (Katsumata & Kamaya, 2003) was downloaded from "Slow Earthquake Database" (Kano et al., 2018; http://www-solid.eps.s.u-tokyo.ac.jp/~sloweq/) supported by JSPS KAKENHI Grant Number JP16H06472 in Scientific Research on Innovative Areas "Science of Slow Earthquakes."

References

Akaike, H. (1980). Likelihood and the Bayes procedure, in Bayesian Statistics, edited by Bernardo, J. M., DeGroot, M. H., Lindley, D. V. and Smith, A. F. M., 143–166, University Press, Valencia.

Ando, M. (1975). Source mechanisms and tectonic significance of historical earthquakes along the Nankai trough, Japan. *Tectonophysics*, *27*, 119–140. https://doi.org/10.1016/0040-1951(75)90102-X

Araki, E., Saffer, D. M., Kopf, A. J., Wallace, L. M., Kimura, T., Machida, Y., Ide, S., & Davis, E. (2017). Recurring and triggered slow-slip events near the trench at the Nankai Trough subduction megathrust. *Science*, *356*(6343), 1157–1160. https://doi.org/10.1126/science.aan3120

Baba, T., Tanioka, Y., Cummins, P. R. & Uhira, K. (2002). The slip distribution of the 1946 Nankai earthquake estimated from tsunami inversion using a new plate model. *Phys. Earth Planet. Inter.*, *132*, 59–73.

Bartlow, N. M. (2020). A long-term view of Episodic Tremor and Slip in Cascadia. *Geophysical Research Letters*, *47*, e2019GL085303. https://doi.org/10.1029/2019GL085303

Beall, A., Fagereng, Å., & Ellis, S. (2019). Strength of strained two-phase mixtures: Application to rapid creep and stress amplification in subduction zone Mélange. *Geophysical Research Letters*, *46*, 169–178. https://doi.org/10.1029/2018GL081252

Bekaert, D. P. S., Hooper, A. & Wright, T. J. (2015). Reassessing the 2006 Guerrero slow-slip event, Mexico: Implications for large earthquakes in the Guerrero Gap. *Journal of Geophysical Research: Solid Earth*, *120*, 1357–1375. https://doi.org/10.1002/2014JB011557

Behr, W. M., Kotowski, A. J., & Ashley, K. T. (2018). Dehydration - induced rheological heterogeneity and the deep tremor source in warm subduction zones. *Geology*, *46*, 475–478. https://doi.org/10.1130/G40105.1

Central Disaster Management Council (2001). The Central Disaster Management Council of the Japanese government, Tokyo. (Available at http://www.bousai.go.jp/jishin/chubou/20011218/siryou2-2.pdf)

Fagereng, A. & Sibson, R. H. (2010), Mélange rheology and seismic style. *Geology*, *38*(8), 751– 754. https://doi.org/10.1130/G30868.1

Fagereng, Å., Hillary, G. W. B., & Diener, J. F. A. (2014). Brittle-viscous deformation, slow slip, and tremor. *Geophysical Research Letters*, *41*, 4159–4167. https://doi.org/10.1002/2014GL060433

Frank, W. B., Radiguet, M, Rousset, B, Shapiro, NM, Husker, AL, Kostoglodov, V, Cotte, N, & Campillo, M (2015), Uncovering the geodetic signature of silent slip through repeating earthquakes. *Geophysical Research Letters*, *42*, 2774–2779. https://doi.org/10.1002/2015GL063685

Frank, W. B. (2016), Slow slip hidden in the noise: The intermittence of tectonic release, *Geophysical Research Letters*, *43*, 10,125–10,133. https://doi.org/10.1002/2016GL069537.

Gao, X., & Wang, K. (2017). Rheological separation of the megathrust seismogenic zone and episodic tremor and slip. *Nature*, *543*, 416–419. https://doi.org/10.1038/nature21389

Graham, S. E., DeMets, C., Cabral-Cano, E., Kostoglodov, V., Walpersdorf, A., Cotte, N., et al. (2014). GPS constraints on the 2011–2012 Oaxaca slow slip event that preceded the 2012 March 20 Ometepec earthquake, southern Mexico. *Geophysical Journal International*, *197*(3), 1593–1607. https://doi.org/10.1093/gji/ggu019

Haines, J., Wallace, L. M., & Dimitrova, L. (2019). Slow slip event detection in Cascadia using vertical derivatives of horizontal stress rates. *Journal of Geophysical Research: Solid Earth*, *124*, 5153–5173. https://doi.org/10.1029/2018JB016898

Hall, K., Houston, H., & Schmidt, D. (2018). Spatial comparisons of tremor and slow slip as a constraint on fault strength in the northern Cascadia subduction zone. *Geochemistry, Geophysics, Geosystems*, *19*, 2706–2718. https://doi.org/10.1029/2018GC007694

Hirose, F., Nakajima, J. & Hasegawa, A. (2008). Three-dimensional seismic velocity structure and configuration of the Philippine Sea slab in southwestern Japan estimated by double-difference tomography. *Journal of Geophysical Research*, *113*, B09315, https://doi.org/10.1029/2007JB005274

Hirose, H., Hirahara, K., Kimata, F., Fujii, N., & Miyazaki, S. (1999). A slow thrust slip event following the two 1996 Hyuganada earthquakes beneath the Bungo Channel, southwest Japan. *Geophysical Research Letters*, *26*(21), 3237–3240. https://doi.org/10.1029/1999GL010999

Hirose, H., & Obara, K. (2010), Recurrence behavior of short-term slow slip and correlated nonvolcanic tremor episodes in western Shikoku, southwest Japan, *Journal of Geophysical Research*, *115*, B00A21, https:/doi.org/10.1029/2008JB006050.

Hooper, A., Bekaert, D., Spaans, K., & Ankan, M. (2012). Recent advances in SAR interferometry time series analysis for measuring crustal deformations. *Tectonophysics*, *514–517*, 1–13. https://doi.org/10.1016/j.tecto.2011.10.013

Ide, S., Beroza, G. C., Shelly, D. R., & Uchide, T. (2007). A scaling law for slow earthquakes. *Nature*, *447*(7140), 76–79. https://doi.org/10.1038/nature05780

Itaba, S., Koizumi, N., Matsumoto, N. *et al.* (2010). Continuous Observation of Groundwater and Crustal Deformation for Forecasting Tonankai and Nankai Earthquakes in Japan. *Pure Appl. Geophys. 167*, 1105–1114. https://doi.org/10.1007/s00024-010-0095-z

Ito, Y., Hino, R., Kido, M., Fujimoto, H., Osada, Y., Inazu, D., et al. (2013). Episodic slow slip events in the Japan subduction zone before the 2011 Tohoku-Oki earthquake. *Tectonophysics*, *600*, 14–26. https://doi.org/10.1016/j.tecto.2012.08.022

Kano, M., Aso, N., Matsuzawa, T., Ide, S., Annoura, S., Arai, R., et al. (2018). Development of a Slow Earthquake Database, *Seismological Research Letters*, *89*(4), 1566–1575, https:/doi.org/10.1785/0220180021.

Kano, M., Kato, A. & Obara, K. (2019), Episodic tremor and slip silently invades strongly locked megathrust in the Nankai Trough. *Scientific Reports*, *9*, 9270. https://doi.org/10.1038/s41598-019-45781-0

Kato, A., Obara, K., Igarashi, T., Tsuruoka, H., Nakagawa, S., & Hirata, N. (2012), Propagation of slow slip leading up to the 2011Mw9.0Tohoku-oki earthquake. *Scienc*e, *335*, 705–708.

545 Kato, A., Fukuda, J., & Obara, K. (2013), Response of seismicity to static and dynamic stress
546 changes induced by the 2011 *M*9.0 Tohoku-Oki earthquake, *Geophysical Research*
547 *Letters*, *40*, 3572– 3578, https://doi.org/10.1002/grl.50699
548 Katsumata, A., & Kamaya, N. (2003), Low-frequency continuous tremor around the Moho
549 discontinuity away from volcanoes in the southwest Japan, *Geophysical Research Letters*,
550 *30*(1), 1020, https://doi.org/10.1029/2002GL0159812
551 Kobayashi, A. (2014). A long-term slow slip event from 1996 to 1997 in the Kii Channel,
552 Japan. *Earth, Planets and Space*, *66*(1), 9.
553 Kobayashi, A. (2017). Objective detection of long-term slow slip events along the Nankai
554 Trough using GNSS data (1996–2016). *Earth, Planets and Space*, *69*(1), 171.
555 https://doi.org/10.1186/s40623-017-0755-7
556 Miyazaki, S., & Heki, K. (2001). Crustal velocity field of southwest Japan. *Journal of*
557 *Geophysical Research*, *106*(B3), 4305–4326. https://doi.org/10.1029/2000JB900312
558 Miyazaki, S., Segall, P., McGuire, J. J., Kato, T., & Hatanaka, Y. (2006). Spatial and
559 temporal evolution of stress and slip rate during the 2000 Tokai slow earthquake. *Journal*
560 *of Geophysical Research*, *111*, B03409. https://doi.org/10.1029/2004JB003426
561 Nakagawa, H. et al. (2009). Development and validation of GEONET new analysis strategy
562 (Version 4), *J. Geogr. Surv. Inst.*, *118*, 1–8 (in Japanese).
563 Nakajima, J. & Hasegawa, A. (2007). Subduction of the Philippine Sea plate beneath
564 southwestern Japan: Slab geometry and its relationship to arc magmatism. *Journal of*
565 *Geophysical Research*, *112*, B08306, https://doi.org/10.1029/2006JB004770
566 National Research Institute for Earth Science and Disaster Resilience (2019). NIED Hi-net,
567 https://doi.org/10.17598/nied.0003

568 Nishimura, T. (2009). Slip distribution of the 1973 Nemuro-oki earthquake estimated from
569 the re-examined geodetic data. *Earth Planets and Space*, *61*, 1203–1214,
570 https://doi.org/10.1186/BF03352973
571 Nishimura, T., Matsuzawa, T., & Obara, K. (2013), Detection of short-term slow slip events
572 along the Nankai Trough, southwest Japan, using GNSS data, *Journal of Geophysical*
573 *Research: Solid Earth*, *118*, 3112–3125, https://doi.org/10.1002/jgrb.50222
574 Nishimura, T., Yokota, Y., Tadokoro, K., & Ochi, T. (2018). Strain partitioning and
575 interplate coupling along the northern margin of the Philippine Sea plate, estimated from
576 Global Navigation Satellite System and Global Positioning System-Acoustic data.
577 *Geosphere*, 14(2), 1–17. https://doi.org/10.1130/GES01529.1
578 Obara, K., Hirose, H., Yamamizu, F., & Kasahara, K. (2004). Episodic slow slip events
579 accompanied by non-volcanic tremors in southwest Japan subduction zone. *Geophysical*
580 *Research Letters*, *31*, L23602. https://doi.org/10.1029/2004GL020848
581 Obara, K., & Kato, A. (2016). Connecting slow earthquakes to huge earthquakes. *Science*,
582 *353*(6296), 253–257. https://doi.org/10.1126/science.aaf1512
583 Ochi, T., & Kato, T. (2013). Depth extent of the long-term slow slip event in the Tokai
584 district, central Japan, A new insight. *Journal of Geophysical Research: Solid Earth*, *118*,
585 1–14. https://doi.org/10.1002/jgrb.50355
586 Okada, Y. (1992). Internal deformation due to shear and tensile faults in a half-space. *Bull.*
587 *Seismol. Soc. Am.*, *82*, 1018–1040.
588 Ozawa, S., Murakami, M., & Tada, T. (2001). Time-dependent inversion study of the slow
589 thrust event in the Nankai trough subduction zone, southwestern Japan. *Journal of*
590 *Geophysical Research*, *106*(B1), 787–802. https://doi.org/10.1029/2000JB900317
591 Ozawa, S., Nishimura, T., Munekane, H., Suito, H., Kobayashi, T., Tobita, M., & Imakiire,
592 T. (2012), Preceding, coseismic, and postseismic slips of the 2011 Tohoku earthquake,

Japan, *Journal of Geophysical Research: Solid Earth*, *117*, B07404, https://doi.org/10.1029/2011JB009120

Ozawa, S., Yarai, H., Imakiire, T., & Tobita, M. (2013). Spatial and temporal evolution of the long-term slow slip in the Bungo Channel, Japan. *Earth, Planets, and Space*, *65*(2), 67–73. https://doi.org/10.5047/eps.2012.06.009

Ozawa, S., Tobita, M., & Yarai, H. (2016). A possible restart of an interplate slow slip adjacent to the Tokai seismic gap in Japan. *Earth, Planets and Space*, *68*(1), 1–14. https://doi.org/10.1186/s40623-016-0430-4

Radiguet, M., Perfettini, H., Cotte, N. *et al.* Triggering of the 2014 M_w7.3 Papanoa earthquake by a slow slip event in Guerrero, Mexico. *Nature Geosciences*, *9*, 829–833. https://doi/org/10.1038/ngeo2817

Rousset, B., Campillo, M., Lasserre, C., Frank, W. B., Cotte, N., Walpersdorf, A., et al. (2017). A geodetic matched-filter search for slow slip with application to the Mexico subduction zone. *Journal of Geophysical Research: Solid Earth*, 122, 10,498–10,514. https://doi.org/10.1002/2017JB014448

Ruina, A. (1983). Slip instability and state variable friction laws. *Journal of Geophysical Research*, *88*(B12), 10,359–10,370. https://doi.org/10.1029/JB088iB12p10359

Ruiz, S., Metois, M., Fuenzalida, A., Ruiz, J., Leyton, F., Grandin, R., Vigny, C., Madariaga, R., & Campos, J. (2014). Intense foreshocks and a slow slip event preceded the 2014 Iquique M_w 8.1 earthquake. *Science*, *345*, 1165–1169. https://doi.org/10.1126/science.1256074

Sagiya, T., & Thatcher, W. (1999). Coseismic slip resolution along a plate boundary megathrust: The Nankai Trough, southwest Japan. *Journal of Geophysical Research*, *104*(B1), 1111–1129.

Sakaue, H., Nishimura, T., Fukuda, J., & Kato, T. (2019). Spatiotemporal evolution of long- and short-term slow slip events in the Tokai region, central Japan, estimated from a very dense GNSS network during 2013–2016. *Journal of Geophysical Research: Solid Earth, 124*. https://doi.org/10.1029/2019JB018650

Schwartz, S. Y., & Rokosky, J. M. (2007), Slow slip events and seismic tremor at circum-Pacific subduction zones, *Rev. Geophys., 45*, RG3004, https://doi.org/10.1029/2006RG000208

Sekine, S., Hirose, H., & Obara, K. (2010), Along-strike variations in short-term slow slip events in the southwest Japan subduction zone, *Journal of Geophysical Research, 115*, B00A27, https://doi.org/10.1029/2008JB006059.

Shelly, D. R., Beroza, G. C., & Ide, S. (2007). Non-volcanic tremor and low-frequency earthquake swarms. *Nature*, *446*(7133), 305–307. https://doi.org/10.1038/nature05666

Socquet, A., Valdes, J. P., Jara, J., Cotton, F., Walpersdorf, A., Cotte, N., Specht, S., Ortega-Culaciati, F., Carrizo, D., & Norabuena, E. (2017), An 8 month slow slip event triggers progressive nucleation of the 2014 Chile megathrust, *Geophysical Research Letters*, *44*, 4046– 4053, https://doi.org/10.1002/2017GL073023

Takagi, R., Uchida, N., & Obara, K. (2019). Along-strike variation and migration of long-term slow slip events in the western Nankai subduction zone, Japan. *Journal of Geophysical Research: Solid Earth*, *124*, 3853– 3880. https://doi.org/10.1029/2018JB016738

Voss, N., Dixon, T. H., Liu, Z., Malservisi, R., Protti, M., & Schwartz, S. (2018). Do slow slip events trigger large and great megathrust earthquakes? *Science Advances*, *4*(10), eaat8472. https://doi.org/10.1126/sciadv.aat8472

Wallace, L. M., Webb, S. C., Ito, Y., Mochizuki, K., Hino, R., Henrys, S., Schwartz, S. Y., & Sheehan, A. F. (2016). Slow slip near the trench at the Hikurangi subduction zone, New Zealand. *Science*, *352*(6286), 701–704. https://doi.org/10.1126/science.aaf2349

Wessel, P., & Smith, W. H. F. (1998), New, improved version of Generic Mapping Tools released, Eos Trans. AGU, *79*, 579.

Yokota, Y., & Koketsu, K. (2015). A very long-term transient event preceding the 2011 Tohoku earthquake. *Nature Communications*, *6*(1), 5934. https://doi.org/10.1038/ncomms6934

Yokota, Y., Ishikawa, T., Watanabe, S., Tashiro, T., & Asada, A. (2016). Seafloor geodetic constraints on interplate coupling of the Nankai Trough megathrust zone. *Nature*, *534*, 374– 377. https://doi.org/10.1038/nature17632

Yoshida, S., & Kato, N. (2003). Episodic aseismic slip in a two-degree-of-freedom block-spring model. *Geophysical Research Letters*, *30*(13), 1681. https://doi.org/10.1029/2003GL017439

Tables

Table 1. *List of onsets and moment magnitudes of S-SSEs detected by tiltmeters (Sekine et al. 2010) and GNSS (Nishimura et al., 2013). The reference dates (see section 2) is set when maximum numbers of LFEs occurred around each onset of S-SSEs in (a) eastern Shikoku, (b) Kii, and (c) Tokai regions.*

(a) Eastern Shikoku

Onset of S-SSEs		**LFE_max (Reference date)**	**Moment magnitude (× 10^{17} Nm)**	
Tiltmeters*	**GNSS****		**Tiltmeters***	**GNSS****
	2004/10/21	2004/10/27		11.5

	2004/12/17	2004/12/19		6.1
	2005/11/05	2005/11/07		10.4
	2006/02/21	2006/02/16		8.5
	2006/06/24	2006/06/24		5.3
2006/11/07	2006/11/11	2006/11/09	9.9	13.4
	2007/03/19	2007/03/18		3.4
	2007/05/10	2007/05/06		16.8
	2007/06/21	2007/06/22		6.3
	2007/10/17	2007/10/14		15.0
2008/02/13	2008/02/14	2008/02/15	13.5	9.8
	2008/10/14	2008/10/15		11.5

(b) Kii

Onset of S-SSEs		**LFE_max (Reference date)**	**Moment magnitude (× 10^{17} Nm)**	
Tiltmeters*	**GNSS****		**Tiltmeters***	**GNSS****
2004/11/29		2004/11/29	7.3	
	2005/01/04	2005/01/03		7.3
2005/07/09		2005/07/10	8.3	
2006/01/07	2006/01/10	2006/01/10	13.8	23.6
	2006/03/17	2006/03/15		6.8
2006/05/29		2006/06/01	5.6	
	2006/07/25	2006/07/28		5.8
2006/11/04	2006/11/11	2006/11/05	9.3	15.3
2007/03/23	2007/03/23	2007/03/24	3.7	4.9
	2007/07/23	2007/07/19		11.5
2007/10/16		2007/10/17	2.8	
	2007/11/14	2007/11/15		7.9
2008/03/05	2008/03/07	2008/03/06	7.6	9.0
2008/06/15	2008/06/21	2008/06/18	6.4	13.0

(c) Tokai

Onset of S-SSEs		**LFE_max (Reference date)**	**Moment magnitude (× 10^{17} Nm)**	
Tiltmeters*	**GNSS****		**Tiltmeters***	**GNSS****
2004/12/17	2004/12/20	2004/12/21	6.3	8.8
2005/07/20	2005/07/29	2005/07/20	5.3	6.0

2006/01/16 2006/01/19		2006/01/21	2.2 1.5	
	2006/07/20	2006/07/16		6.0
2006/08/27		2006/08/30	4.8	
2007/02/04	2007/02/09	2007/02/05	4.0	10.2
	2007/08/28	2007/08/29		6.5
2007/09/25 2007/10/05	2007/10/09	2007/10/09	2.8 3.6	7.2
2007/12/31		2008/01/03	7.9	
2008/05/14		2008/05/16	3.9	
	2008/08/21	2008/08/31		8.4

Note. *Sekine et al. (2010), **Nishimura et al. (2013)

Figure Captions

Figure 1. The study area in southwest Japan is indicated by a large rectangle in the inset. The Philippine Sea plate is subducting northeastward beneath the Amurian plate along the Nankai Trough. The black contours indicate the iso-depths of the upper surface of the subducting Philippine Sea plate with an interval of 10 km (Baba et al., 2002; Nakajima & Hasegawa, 2007; Hirose et al., 2008). The red rectangles are the eastern Shikoku, Kii, and Tokai areas, where S-SSEs are investigated in this study. The green lines are the source areas of the 1944 Tonankai and 1946 Nankai earthquakes (Sagiya & Thatcher, 1999) and the aniticipated source area in Tokai proposed by the Central Disaster Management Council (2001). The blue circles indicate the locations of L-SSEs in the Bungo Channel (Hirose et al., 1999), Kii Channel (Kobayashi, 2014), Tokai (Miyazaki et al., 2006), and shallow SSE southeast of Kii (Araki et al., 2017). The black dots show the locations of GEONET stations used in this study.

Figure 2. (Left) Stacked displacement with 2-σ observation errors and (right) examples of detrended GNSS time series in the 4-digit in the left panel in (a) eastern Shikoku, (b) Kii, and (c) Tokai. The red dots are the LFE epicenters. The red and black lines indicate the time

series for the EW and NS components, respectively, cumulated for all S-SSEs detected during the analysis period, while the light red and grey lines are the time series for the individual S-SSE. The displacement vectors during the grey shaded period in the right panel is indicated in the left panel. The detrended time series for all GNSS stations are summarized in Figures S1–S3.

Figure 3. (a) Cumulative slip distribution for 12 S-SSEs in eastern Shikoku inferred by using all stations. The blue rectangles are the fault models from Sekine et al. (2010) and/or Nishimura et al. (2013). The blue circle indicates an L-SSE source area (Kobayashi, 2014). The red dots are LFE epicenters. (b) Same as (a), but the faults where the slips exceeded the estimation error are represented and separated into six (E1–E6) fault patches. The purple lines indicate the contours of the slip deficit rate (Yokota et al., 2016). (c) The comparison between the observed (black arrows) and calculated (blue arrows) displacement vectors. (d) Average slip distribution and (e) its standard deviation for 100 cases, each of which is inverted by randomly choosing 80 % of the GNSS stations.

Figure 4. Calculated displacements due only to the fault slip in (a) E3, (b) E4, (c) E5, and (d) E6 patch, respectively.

Figure 5. (a) Cumulative slip distribution for 14 S-SSEs in Kii region. The blue rectangles are the fault models from Sekine et al. (2010) and/or Nishimura et al. (2013). The red dots represent the LFE locations. (b) Same as (a), but the faults where the slips exceeded the estimation error are represented and separated into two (K1–K2) fault patches. (c) Comparison between the observed (black arrows) and calculated (blue arrows) displacement vectors. (d) Calculated displacements due only to the slip in K2 patch.

709

710 **Figure 6**. (a) Fault slip distribution cumulated for 11 S-SSEs in Tokai region. The blue
711 rectangles are the fault models from Sekine et al. (2010) and/or Nishimura et al. (2013). The
712 red dots indicate the LFE locations. (b) Same as (a), but the subfaults where the slips
713 exceeded the estimation error are indicated. The purple lines indicate the contours of the slip
714 deficit rate (Yokota et al., 2016). The blue circle is the source area of Tokai L-SSE (Miyazaki
715 et al., 2006). (c) Comparison of the observed (black arrows) and calculated (blue arrows)
716 displacements. (d) Calculated displacements due only to the fault slip in the shallow (T2)
717 patch. (e) Fault slip distribution averaged for 100 cases, each of which is inverted by using a
718 random selection of 80 % of the GNSS stations and (f) its estimation error.

719

720 **Figure 7**. Summary of the cumulative slip distribution in southwest Japan and the LFE
721 epicenters in the JMA catalog (Katsumata & Kamaya, 2003). The light blue lines indicate the
722 contours of the LFE densities of 2 (counts) / 0.02 (degree) × 0.02 (degree). The purple lines
723 indicate the contours of the slip deficit rate (Yokota et al., 2016).

Figure 1.

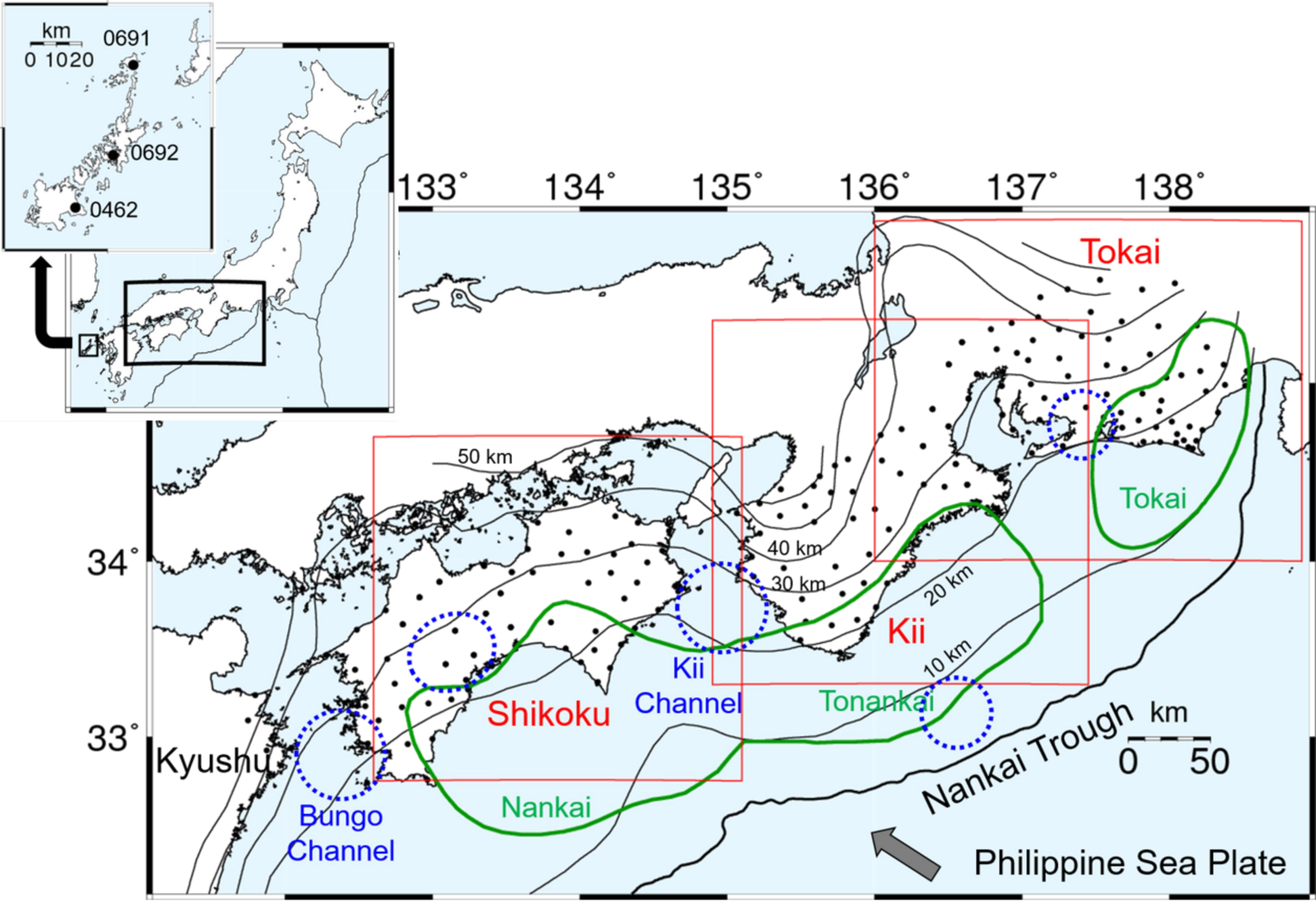
km
0 1020
0691
0692
0462
133˚
134˚
135˚
136˚
137˚
138˚
34˚
33˚
Tokai
Tokai
50 km
40 km
30 km
20 km
10 km
Kii
Kii
Channel
Shikoku
Tonankai
Kyushu
Nankai Trough
km
0 50
Nankai
Bungo
Channel
Philippine Sea Plate

Figure 2.

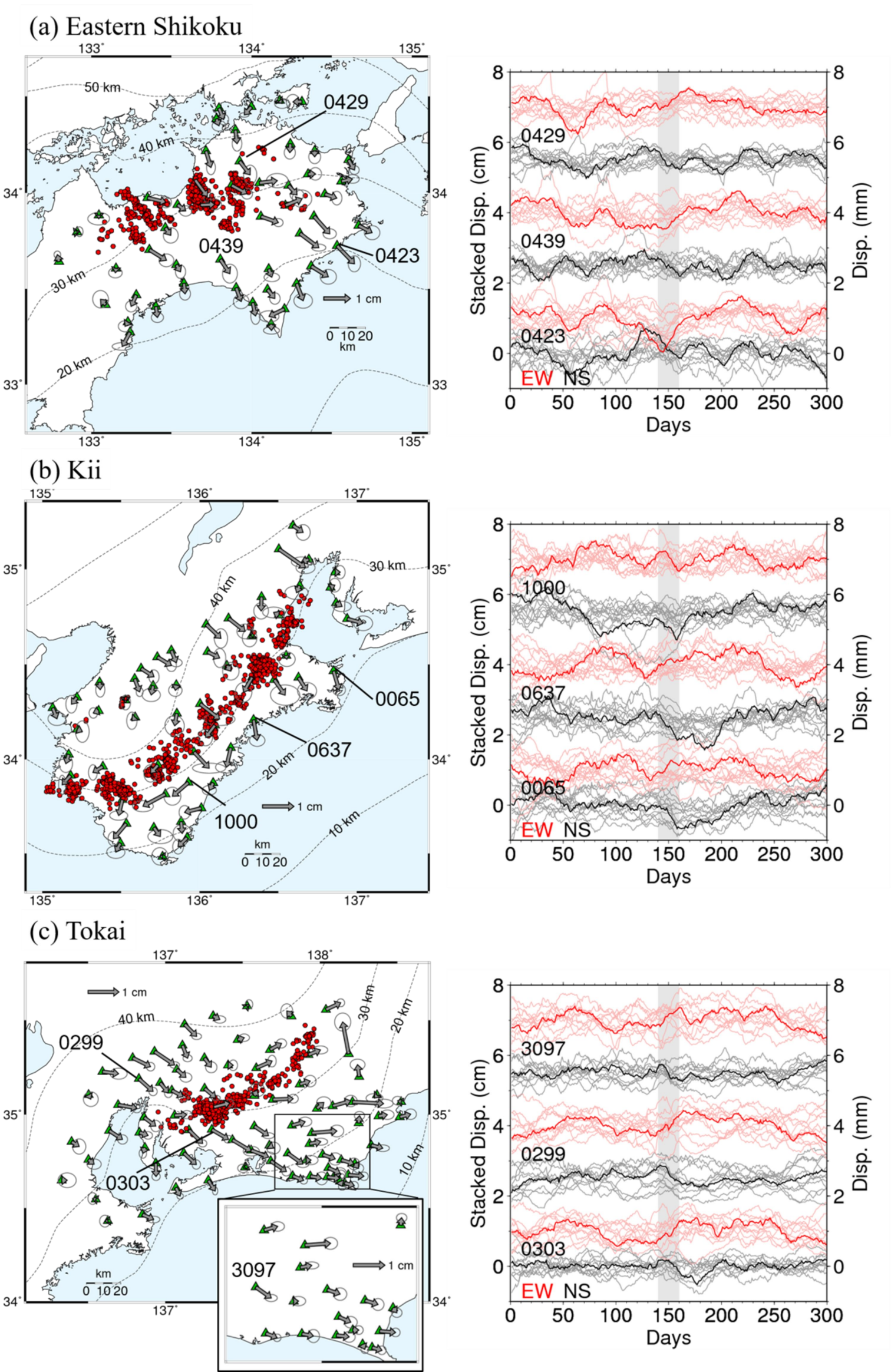
(a) Eastern Shikoku
133°
134°
135°
50 km
40 km
30 km
20 km
0429
0439
0423
1 cm
0 10 20
km
34°
33°
Stacked Disp. (cm)
Disp. (mm)
0429
0439
0423
EW NS
0 50 100 150 200 250 300
Days
(b) Kii
135°
136°
137°
30 km
40 km
20 km
10 km
0065
0637
1000
1 cm
km
0 10 20
35°
34°
1000
0637
0065
EW NS
Days
(c) Tokai
137°
138°
1 cm
40 km
30 km
20 km
10 km
0299
0303
3097
km
0 10 20
35°
34°
3097
0299
0303
EW NS
Days

Figure 3.

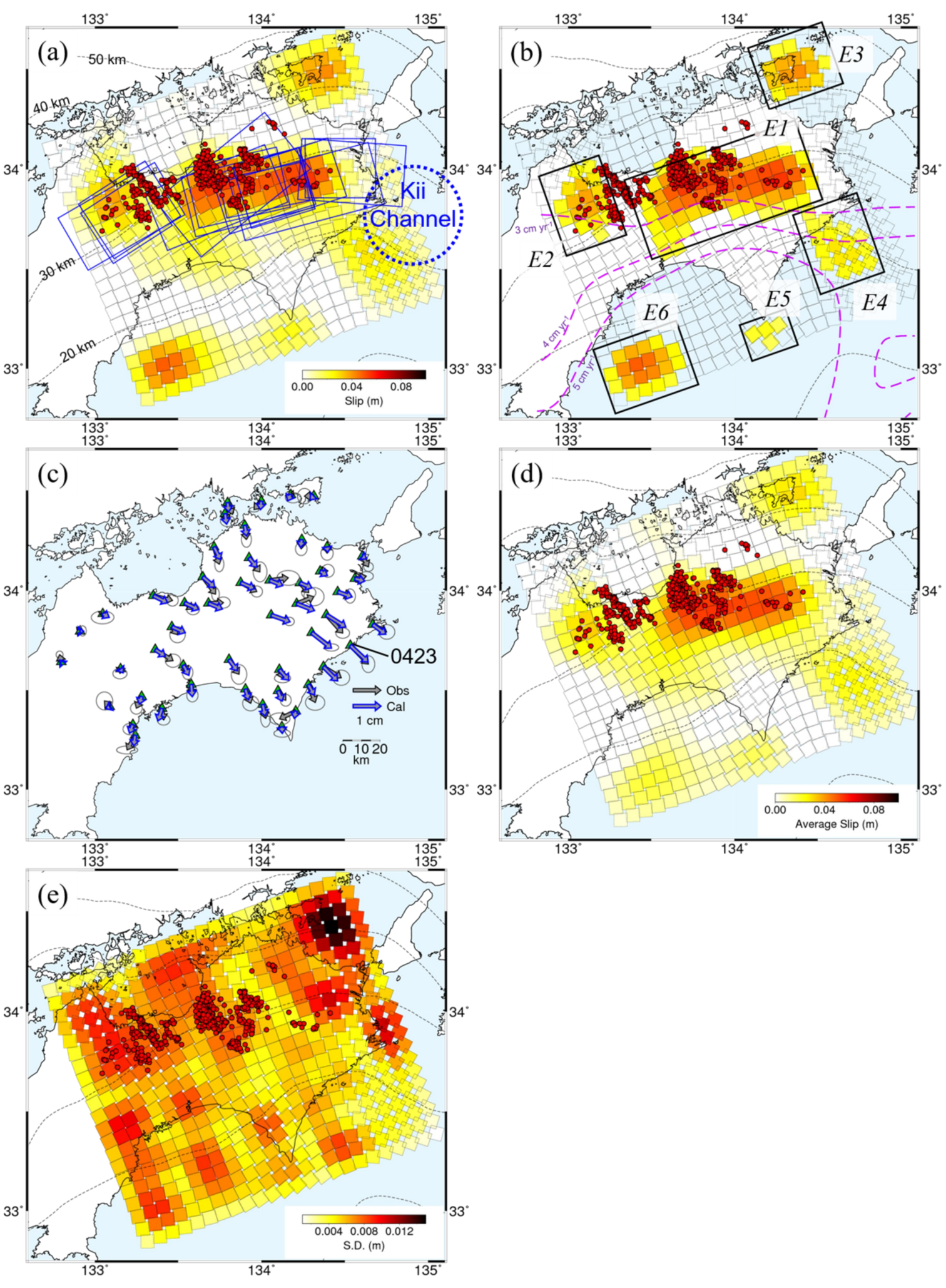
(a)
50 km
40 km
30 km
20 km
Kii
Channel
0.00 0.04 0.08
Slip (m)
(b)
E1
E2
E3
E4
E5
E6
3 cm yr-1
4 cm yr-1
5 cm yr-1
(c)
0423
Obs
Cal
1 cm
0 10 20
km
(d)
0.00 0.04 0.08
Average Slip (m)
(e)
0.004 0.008 0.012
S.D. (m)
133°
134°
135°
34°
33°

Figure 4.

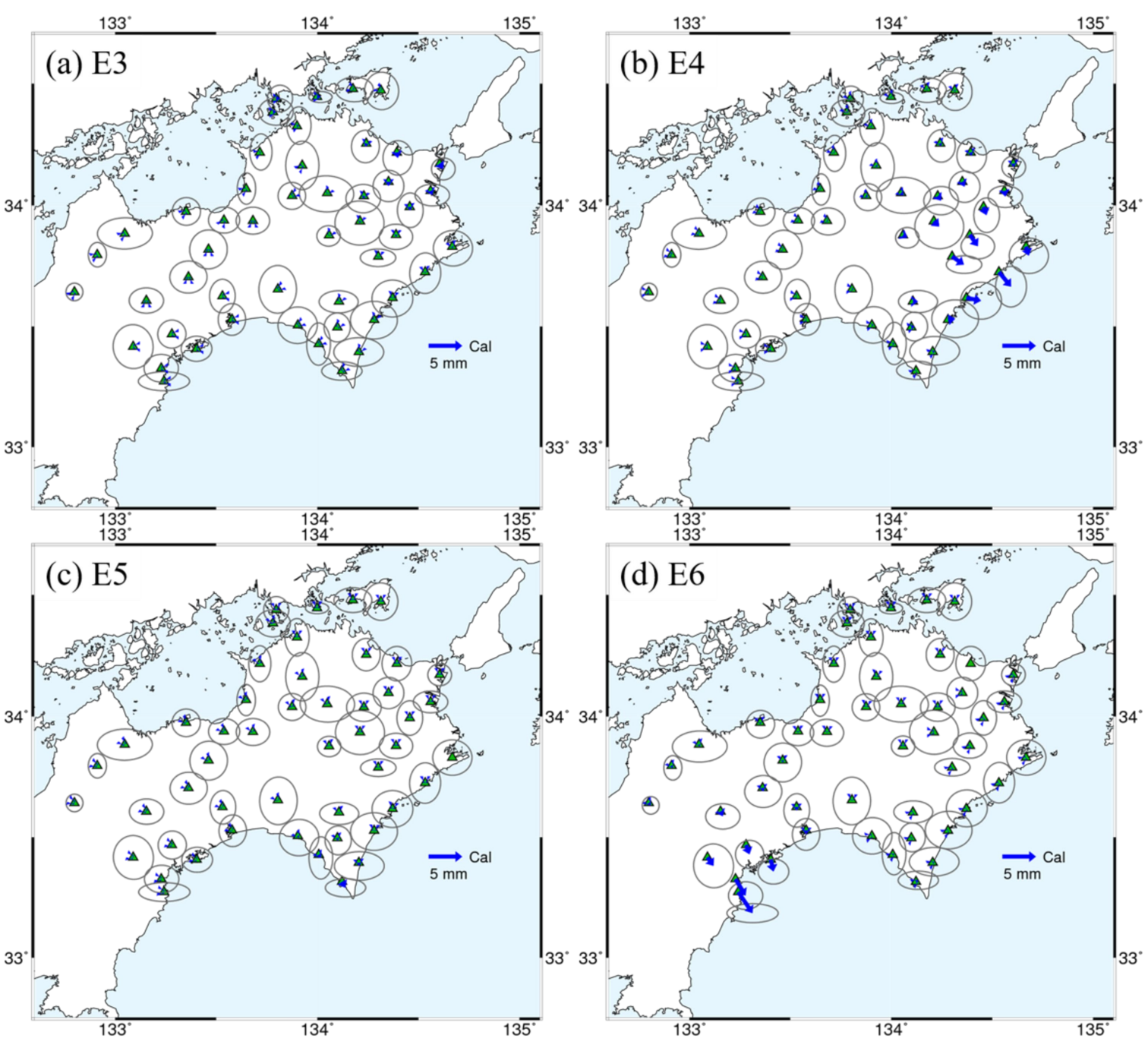
(a) E3
(b) E4
(c) E5
(d) E6
133°
134°
135°
34°
33°
Cal
5 mm

Figure 5.

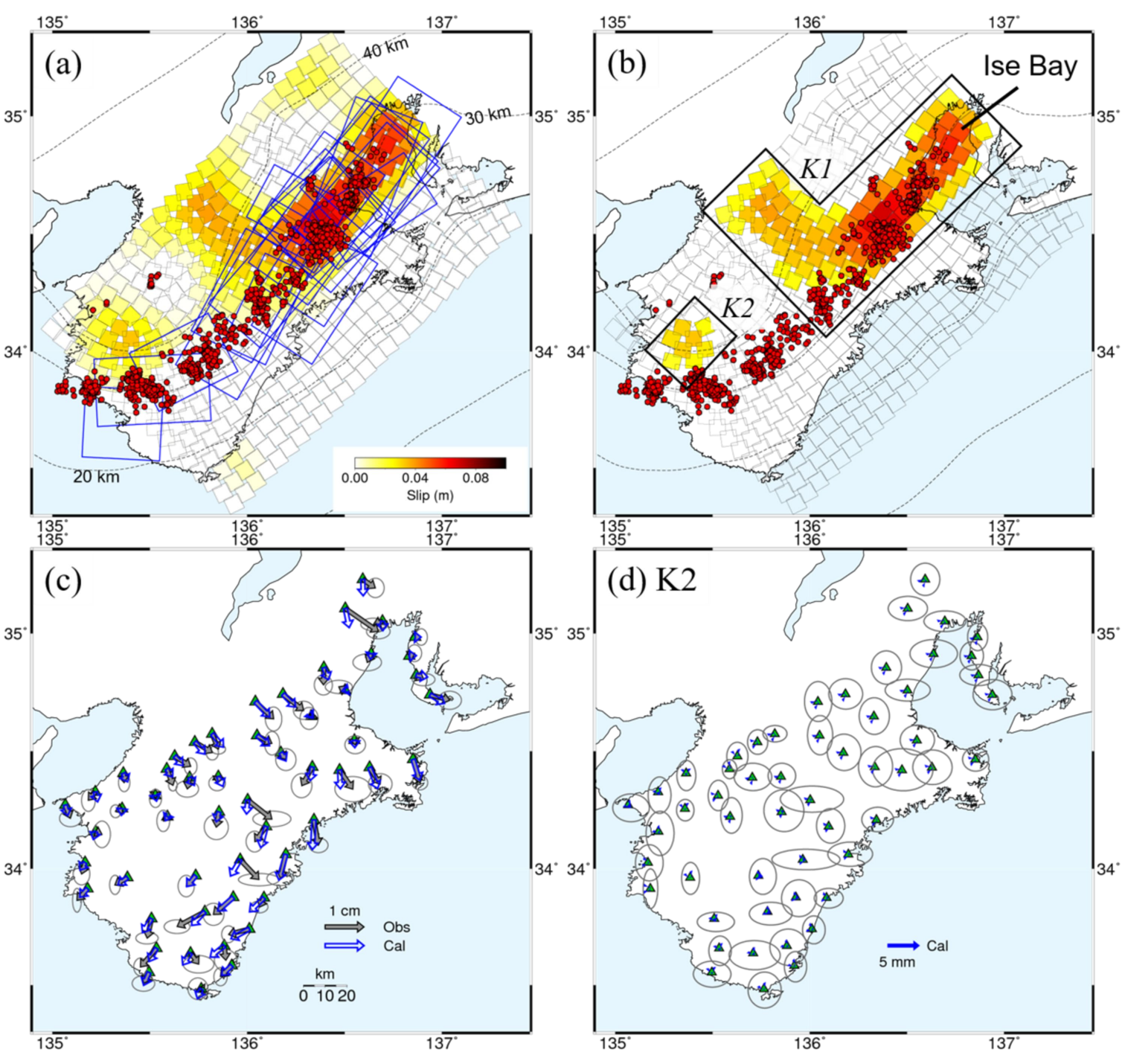
(a)
40 km
30 km
20 km
0.00
0.04
0.08
Slip (m)
(b)
Ise Bay
K1
K2
(c)
1 cm
Obs
Cal
km
0 10 20
(d) K2
Cal
5 mm
135°
136°
137°
35°
34°

Figure 6.

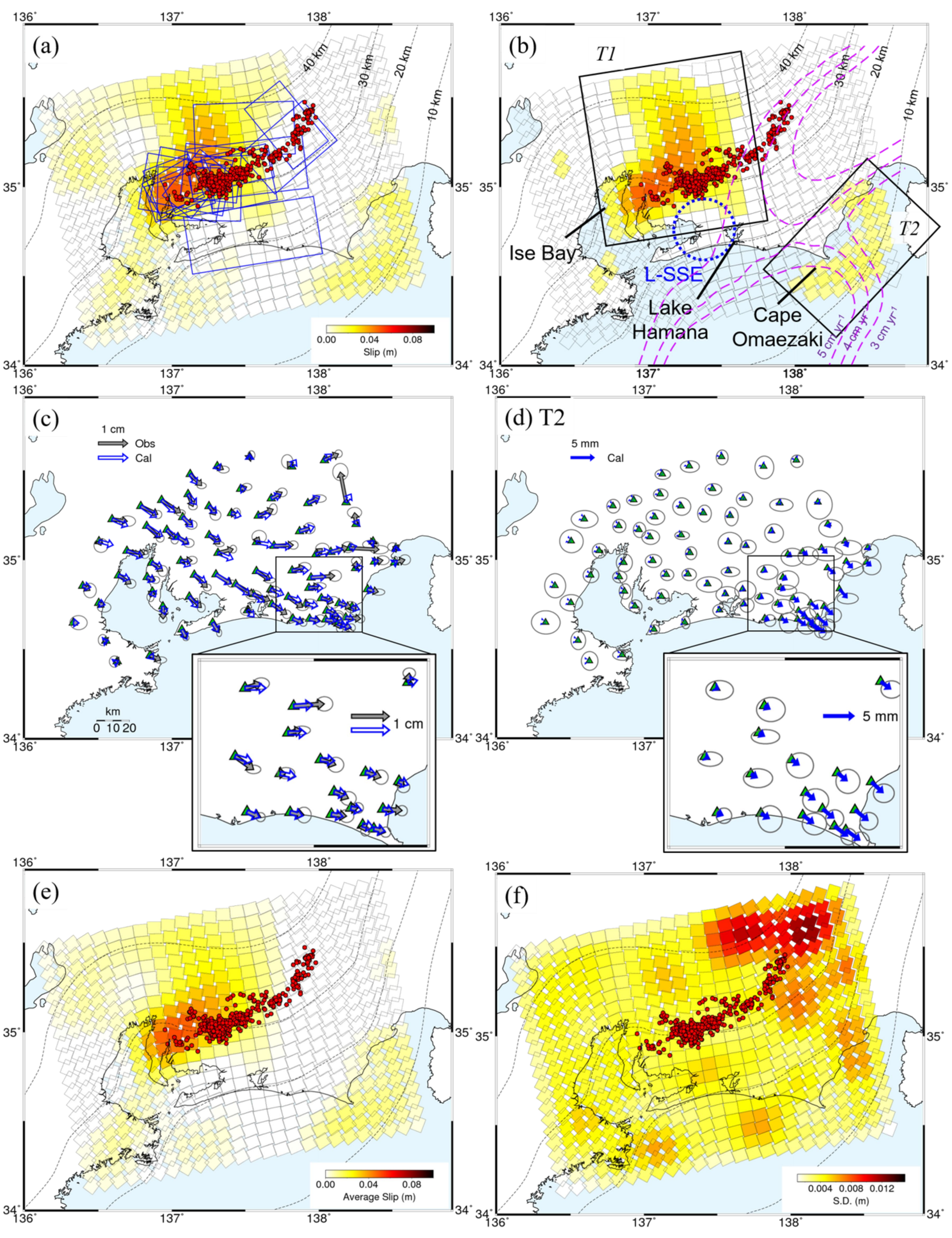
(a)
40 km
30 km
20 km
10 km
0.00 0.04 0.08
Slip (m)
(b)
T1
T2
Ise Bay
L-SSE
Lake Hamana
Cape Omaezaki
5 cm yr-1
4 cm yr-1
3 cm yr-1
(c)
1 cm
Obs
Cal
km
0 10 20
1 cm
(d) T2
5 mm
Cal
5 mm
(e)
0.00 0.04 0.08
Average Slip (m)
(f)
0.004 0.008 0.012
S.D. (m)
136°
137°
138°
34°
35°

Figure 7.

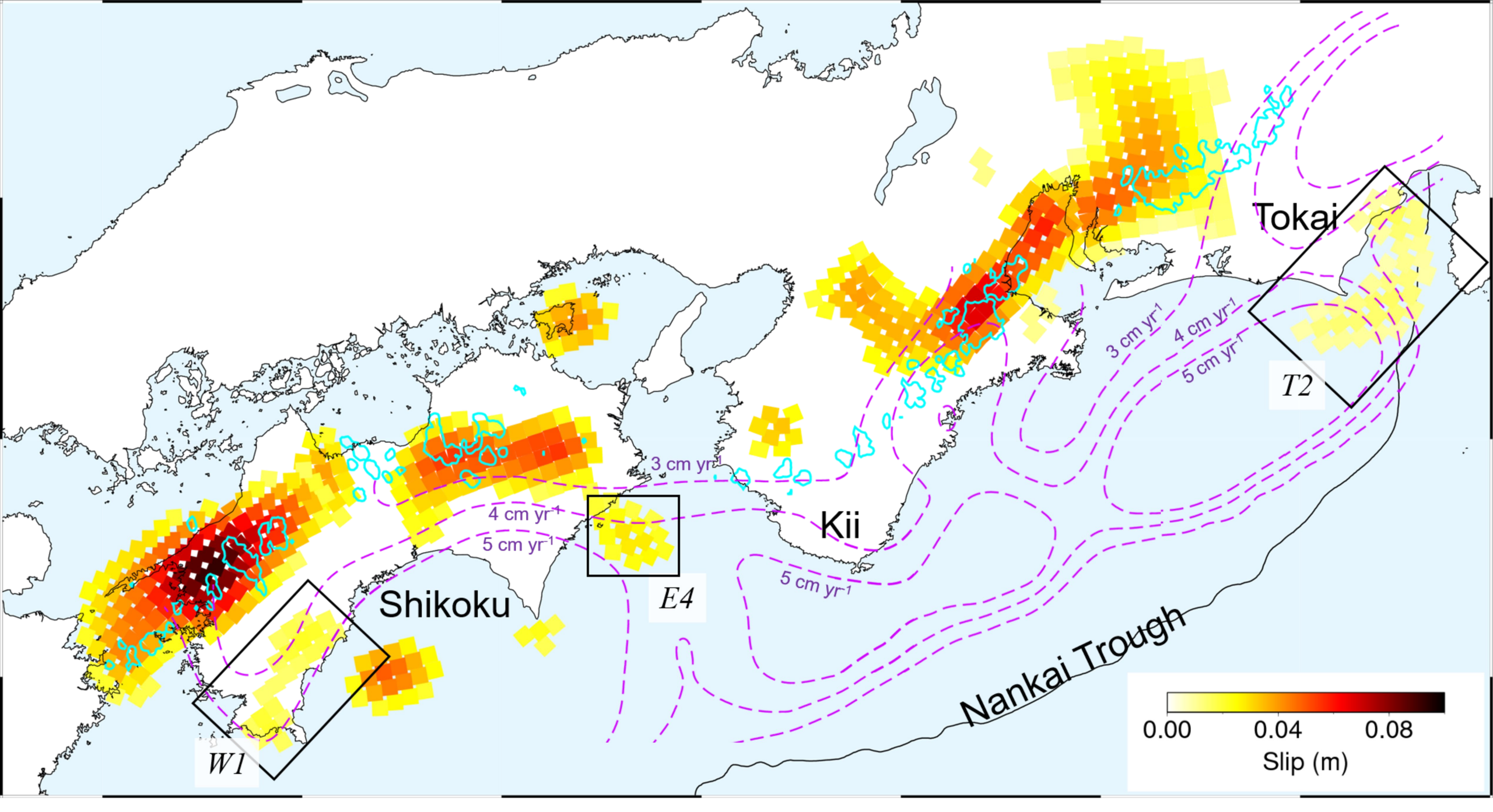
Tokai
T2
3 cm yr-1
4 cm yr-1
5 cm yr-1
Kii
3 cm yr-1
4 cm yr-1
5 cm yr-1
E4
Shikoku
W1
Nankai Trough
0.00
0.04
0.08
Slip (m)